Coarse-Grained Molecular Dynamics Simulations of a Rotating Bacterial Flagellum

Anton Arkhipov,*[†] Peter L. Freddolino,[†‡] Katsumi Imada,[§¶] Keiichi Namba,[§¶] and Klaus Schulten*[†‡]

*Department of Physics, [†]Beckman Institute for Advanced Science and Technology, [‡]Center for Biophysics and Computational Biology, University of Illinois at Urbana-Champaign, Urbana, Illinois; [§]Graduate School of Frontier Biosciences, Osaka University, Osaka, Japan; and [¶]Dynamic Nano Machine Project, International Cooperative Research Project, Japan Science and Technology Agency, Tokyo, Japan

ABSTRACT   Many types of bacteria propel themselves using elongated structures known as flagella. The bacterial flagellar filament is a relatively simple and well-studied macromolecular assembly, which assumes different helical shapes when rotated in different directions. This polymorphism enables a bacterium to switch between running and tumbling modes; however, the mechanism governing the filament polymorphism is not completely understood. Here we report a study of the bacterial flagellar filament using numerical simulations that employ a novel coarse-grained molecular dynamics method. The simulations reveal the dynamics of a half-micrometer-long flagellum segment on a timescale of tens of microseconds. Depending on the rotation direction, specific modes of filament coiling and arrangement of monomers are observed, in qualitative agreement with experimental observations of flagellar polymorphism. We find that solvent-protein interactions are likely to contribute to the polymorphic helical shapes of the filament.

INTRODUCTION

The bacterial flagellum is a large, polymorphic multiprotein assembly used by many types of bacteria to propel themselves through liquid medium. The complete flagellum is made up of three broad domains: a basal body, which acts as an ion-gradient-driven motor; a hook, which acts as a universal joint (curved axle rotating about its center line) in the flagellum; and a filament, which makes up the bulk of the length of the flagellum and interacts with solvent to propel the bacterium (1). The flagellar filament behaves differently depending on the direction of the torque applied by the basal body. Under counter-clockwise rotation (as viewed from the exterior of the cell), several flagella form a single helical bundle (composed of left-handed helices) that acts to propel the cell along a straight line; this is known as the running-mode of motion. Under clockwise rotation, the individual filaments dissociate from the bundle and form separate right handed helices, causing the cell to rotate in place; this is known as the tumbling mode (2). The filament itself forms one of several supercoils, depending on the rotation of the motor; these supercoils have been extensively classified, and generally fall into the normal form for the running mode of motion, and one of the semicoil, curly I, and curly II forms in the tumbling mode (3,4). Varying the duration of running and tumbling modes, bacteria can move up or down a stimulus gradient by a biased random walk (2).

In this study, we concentrate on the flagellar filament of *Salmonella typhimurium*, which has been well characterized in experiments and for which a combined x-ray crystal/cryo-EM structure is available (5–7). This structure is composed of multiple copies (monomers) of a single protein, flagellin. The filament is formed by the helical arrangement of these monomers along its axis, with 11 monomers per turn. For the purposes of understanding filament behavior, it is generally much more useful to consider the filament to be composed of 11 intertwined protofilaments; each protofilament is a stack of monomers that forms a long-pitch coil along the length of the filament. Note that these two representations are identical; each protofilament is simply the subset of monomers occupying identical positions in their respective turns of the overall filament helix.

Early theoretical work on the flagellum suggested that the observed supercoiling forms of flagella arise from the 11 protofilaments individually assuming a so-called short or long conformation. These are defined as such since the interface of subsequent monomers in a protofilament (and adjacent monomers in other protofilaments) can take on two conformations that lead to slightly different spacings between these monomers along the length of the protofilament, without significant internal changes to each monomer. This rearrangement of protofilaments can also give rise to supercoiling of the filament, in which case the location of the short protofilaments becomes the inner face of the supercoil and the location of the longer protofilaments becomes the outer face (8,9). X-ray fiber diffraction studies on straight filaments confirmed the existence of two protofilament forms in the cases where all protofilaments in a filament took on either the long or short conformation; the structure with long-type interfaces formed left-handed helices (and thus this protofilament conformation was denoted *L*) and the shorter type formed right-handed helices (with a protofilament conformation denoted *R*) (10). Theoretical models of filaments containing varying numbers of protofilaments with each of these interface types resulted in supercoils very close to those

observed experimentally; the normal supercoil, for instance, corresponds to a filament with two R and nine L protofilaments (denoted 2*R*/9*L*) (10). This correspondence gave rise to the so-called bistable-protofilament model for flagellar supercoiling, in which different supercoiling forms are thought to arise due to the presence of different ratios of L- and R-type protofilaments. In this model, the interface type is thought to remain uniform through any given protofilament (10,11). Recent molecular dynamics (MD) simulations (12) have suggested an atomic level mechanism for the L-R distinction, based on the presence of a set of ''switch'' interactions formed in L, but not R, protofilaments.

Despite extensive theoretical and experimental studies, the mechanisms responsible for inducing polymorphic transitions in protofilament arrangement between the running and tumbling modes remain unclear. The chiral nature of the flagellin monomers, which show a scooplike curvature (see Fig. 1) on the section interacting with solvent, offers a tantalizing clue on how the filament may interact differently with solvent under different rotational directions. One expects that the friction experienced by the filament differs substantially between the opposite rotation directions, which could then lead to a rearrangement of protofilaments and, hence, to different supercoiling patterns. However, this effect has not been quantified, because the resolution in experiments with functioning flagella is not high enough, the structure is too large to do atomistic simulations easily, and it seems to be too complex for a simple mathematical model description. It is even unclear if the solvent does play an important role for the polymorphic transition. Indeed, recent studies (10,12,13) have focused only on the role of protein-protein interactions, and it is possible that only these internal interactions control filament supercoiling. Thus, there is a need to model the behavior of the flagellar filament on a scale where supercoiling may be observed, but the interactions between the single protein monomers are also resolved. To this end, we have developed a new coarse-grained (CG) MD approach for large biomolecular assemblies, and applied it to the bacterial flagellum.

CG simulations of macromolecular assemblies are becoming increasingly popular and, for example, have recently been used to study large-scale motions of ribosomes (14,15), viral capsids and their elements (16,17), the elasticity of actin filaments (18), lipid bilayers (19,20–22), and the aggregation of lipoprotein particles (23,24). The flagellar filament seems to be an ideal system to apply a CG technique to (12). Its structure is known; it consists of multiple copies of a single protein, the flagellin monomer (making it relatively easy to parameterize); and reliable experimental data are available for comparison. Addressing many aspects of flagellar filament dynamics using traditional all-atom MD would require simulations of tens of millions of atoms for timescales on the order of micro- to milliseconds; both the time and size scales are several orders of magnitude beyond what is currently feasible.

Our CG model (presented below) uses 15 point masses to represent each monomer (flagellin), and the assembly is then simulated with a simple implicit solvent model that accounts for protein-solvent interaction through a frictional term added to the MD description. The number of considered degrees of freedom is ~4000 times smaller than for the all-atom model with explicit solvent, and the integration time step can be raised substantially leading to faster simulation. In fact, we were able to simulate 0.5-μm segments of flagellar filament for tens of microseconds to study the effects of varying torque and solvent conditions on flagellar dynamics. Although quantitative agreement with experimental results is still relatively poor due to the very high speed at which we needed to rotate the model filament, the flagellar motion we observe is qualitatively consistent with the experimentally observed behavior of the filament and the bistable protofilament
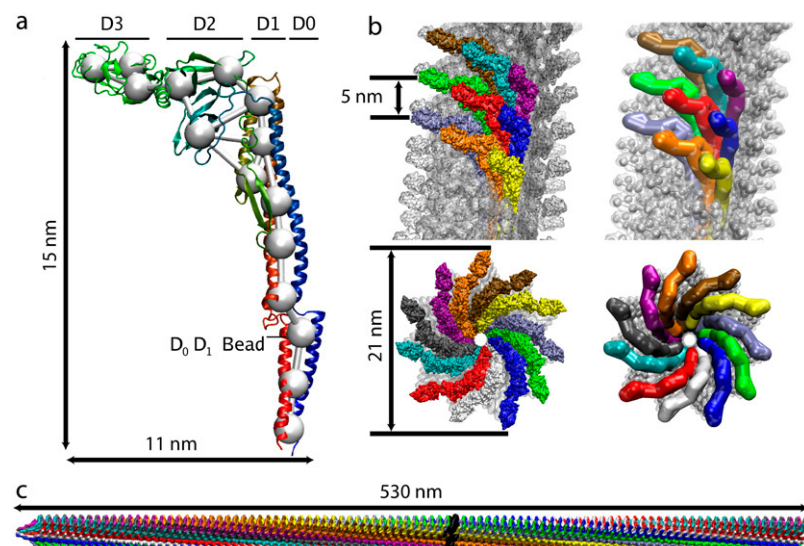

FIGURE 1 Coarse-graining scheme for the flagellar filament. In panel *a*, a flagellin monomer is shown in both all-atom (*cartoon*) and CG (*white beads*) representations. The CG model consists of 15 beads placed according to the mass distribution in the protein; two beads are bonded if the distance between them is <25 Å. The different domains of the flagellin monomer are noted (*top*). In panel *b*, the flagellar filament viewed from the side and from the top is shown in all-atom (*left*) and CG (*right*) representations. A few monomers are highlighted in various colors, to demonstrate the arrangement of monomers comprising the filament. The longest simulated filament segment (1100 monomers) is shown in CG representation in panel *c*. The filament is built of monomers arranged in a helical fashion, 11 proteins per helix turn (single helix turn is highlighted in *black*). The 11 protofilaments, all in the R state, are drawn in differing colors.

model. In particular, we find that solvent viscosity should play a key role in inducing transitions between different coiling and supercoiling states of the filament.

In this article, we define coiling as the twist observed within the individual protofilaments of the structure about the center of the filament, and supercoiling as twist of the entire filament.

METHODS

The CG method used in this study has been developed in a general form and, accordingly, can be applied to any macromolecular system. A protein (or any other molecule) is represented by a set of CG beads (point masses). Using an all-atom model of a molecule, a given number of CG beads are assigned their positions. Effective interaction potentials between the beads are introduced, using the all-atom simulations to infer the parameters for the CG model. The CG system can then be simulated using existing MD programs, originally intended for all-atom simulations.

The developed CG model is designed primarily for simulations of large-scale motions of macromolecular assemblies for which shapes of constituent molecules do not change significantly; for example, refolding of proteins is not accounted for in our CG model. A single protein in the CG representation should behave as an elastic object of definite form, the spatial distribution of CG beads reproducing the shape of the protein. Proteins appear in various shapes, and in many cases, this shape is not compact, but instead consists of several domains connected by relatively thin and disordered links or involves long tails. When reproducing the shape by a number of CG beads, it is important to reconstruct the bulk of the protein's compact regions as well as links and tails. Accordingly, a method which assigns each CG bead to represent the same number of atoms would be inefficient, since either the tails would be misrepresented or the number of CG beads representing compact regions would be too large. Instead, one should use a representation that adapts the beads to the topology of proteins, i.e., three-dimensional bulky bodies, planar sheets, or linear links and tails. In addition, one may want to use a multiresolution method that permits coarser and finer representations in different parts of the macromolecule (protein). Such methods were developed in the field of neural computation (25), and we chose to use one of them, the so-called topology-generating network (26,27).

The algorithm, in its simplest uniform resolution mode, works as follows. For an all-atom model of the protein (a crystal structure) consisting of N_a atoms (total mass M), with coordinates $\mathbf{r}_i$ and masses m_i ($i = 1, 2, \ldots, N_a$), the mass distribution is used as a target probability distribution, $p(\mathbf{r}) = \sum_j (m_j/M) \delta(\mathbf{r} - \mathbf{r}_j)$, for the neural network. The number N_{CG} ($N_{CG} \ll N_a$) of neurons representing $p(\mathbf{r})$ is specified from the start, the neurons being subsequently identified with the beads of the coarse-grained representation. One chooses N_{CG} according to the desired level of coarse-graining (we used a ratio $N_a/N_{CG} = 500$). Initial positions $\mathbf{R}_k$ ($k = 1, 2, \ldots, N_{CG}$) of the beads are assigned randomly. Then N_{step} adaptation steps are carried out in which representative positions for the beads are determined. During each step, three operations are performed. First, a protein atom is chosen randomly (according to the probability $p(\mathbf{r})$); its position $\mathbf{r}$ serves as an input for the next operations. Second, for each CG bead k, one determines the number n_k of CG beads j with $|\mathbf{r} - \mathbf{R}_j| < |\mathbf{r} - \mathbf{R}_k|$. Third, positions of the beads are updated ($k = 1, 2, \ldots, N_{CG}$) according to the rule

$$\mathbf{R}_k^{new} = \mathbf{R}_k^{old} + \epsilon e^{-n_k/\lambda} (\mathbf{r} - \mathbf{R}_k^{old}), \qquad (1)$$

where ϵ and λ at each step u ($u = 0, 2, \ldots, N_{step}$) are represented by the functional form $f_u = f_0 (f_{N_{step}}/f_0)^{u/N_{step}}$, with $\lambda_0 = 0.2\ N_{CG}$, $\lambda_{N_{step}} = 0.01$, $\epsilon_0 = 0.3$, and $\epsilon_{N_{step}} = 0.05$. Usually, $N_{step} = 200\ N_{CG}$ is enough to obtain a well-converged distribution of CG beads. A typical run of this algorithm for flagellin (500 residues, 15 CG beads) takes less than a second of computer time. The CG and all-atom models of the flagellum filament and of a single unit protein are compared in Fig. 1. Once a single protein is coarse-grained,

the distribution of CG beads can be mapped on the other orientations of the same protein; in this way, all unit proteins building up the flagellum filament are coarse-grained identically. Both the coarse-graining and mapping programs were implemented in C++ and can be applied to any other molecular system without changes.

We choose the interaction potentials between the CG beads in the form of the CHARMM force field (28), i.e., bonded interactions are described by harmonic bond and angle potentials (we did not use dihedral potentials), and the nonbonded potentials include only 6–12 Lennard-Jones (LJ) and Coulomb terms. After the positions of CG beads are defined, we find for each atom the CG bead closest to it; the atom then belongs to the domain of this bead, the so-called Voronoi cell. The total mass and charge of each domain are assigned to the corresponding CG bead. Two CG beads are bonded if the distance between them is <25 Å (with this choice, all CG beads representing the flagellin are in one network, but regions that are not connected in the all-atom model remain disconnected in the CG model). Separate monomers interact only through nonbonded forces.

To determine the parameters for bonded interactions, we ran a 7-ns-long, all-atom MD simulation of a single flagellin monomer. Assuming that each bond and angle is an independent harmonic oscillator, and following the distances between the centers of mass of the domains corresponding to certain CG beads, we extracted the equilibrium bond lengths (or angles) and spring constants from the mean distances (angles) and respective root mean-square deviations (RMSD). This procedure can be illustrated by the simple example of a one-dimensional harmonic oscillator, with a particle moving along the x coordinate in the potential $V(x) = f(x - x_0)^2/2$. With the system in equilibrium at temperature T, the average position $\langle x \rangle$ is equal to x_0, and the RMSD is given by $k_B T/f$ (k_B is the Boltzmann constant). Using an MD simulation, one can compute $\langle x \rangle$ and the RMSD, thus obtaining x_0 and f. These formulas change slightly for bonds and angles, but the principle that the two parameters of a harmonic oscillator can be derived from the mean and RMSD of the coordinates, holds. This procedure allows one to systematically obtain suitable values for the interaction parameters.

To parameterize the nonbonded potentials, we chose several segments of the flagellin monomer, ~500 atoms each (roughly representing a single CG bead), and carried out 10 all-atom simulations of various pairs of these segments, for ~10 ns each. The potential of mean force (PMF) between the two segments was obtained for every pair using the Boltzmann inversion method (17,24,29). The PMFs (see Fig. 2) were found to be similar to an LJ potential in shape, and for each pair the well-depth was ~4 kcal/mol.
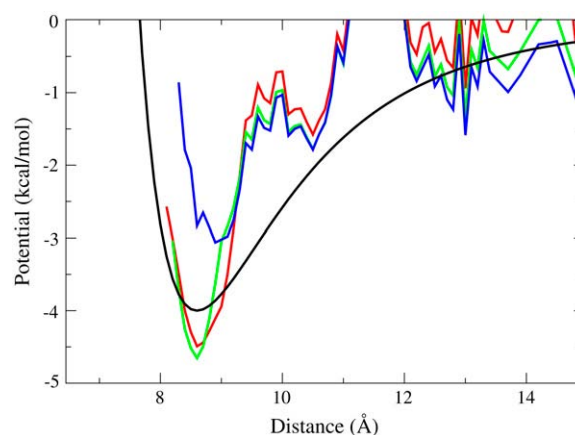

FIGURE 2 Extraction of nonbonded CG potential from the all-atom simulations. Results from one of the several all-atom simulations are shown. The potential of mean force is presented as extracted from a trajectory after 1 ns (*blue*), 5 ns (*green*), and 10 ns (*red*), demonstrating the convergence. The fitted Lennard-Jones 6–12 potential with the well-depth of 4 kcal/mol and the well-minimum position of 8.6 Å is shown in black.

Therefore, the LJ well-depth for each CG bead is set to 4 kcal/mol. The all-atom simulations mentioned here were performed in vacuum, with the total charge of the protein neutralized, because the Coulomb interactions between large charged domains of the protein should be included in the Coulomb interactions between the charged beads, and not in the bonded or LJ interactions. The LJ radius for each CG bead is calculated as the radius of gyration of the respective all-atom domain, increased by 2 Å (approximately an average LJ radius of an atom in the CHARMM force field). This choice was verified by comparison with the PMFs extracted from the all-atom simulations: for each pair of protein segments in those simulations, the position of the PMF minimum was close to the sum of the gyration radii of each segment, increased by 4 Å.

The procedure for constructing the CG nonbonded potentials presented above showed satisfactory convergence and independence from initial conditions of the all-atom simulations. We found that 10 ns was generally enough to obtain a well-converged PMF, as demonstrated by an example in Fig. 2. The influence of the initial conditions on the shape of the PMF in our procedure is not significant, since the values for PMF well-depth were found to be approximately the same (3–5 kcal/mol) in all cases. Similarly, in each simulation the position of the PMF minimum was well represented by the sum of the gyration radii of each segment (adding 4 Å). The uniformity of the obtained PMFs shows that for protein pieces 500 atoms in size, the strength of interactions between such pieces (PMF well-depth) is rather nonspecific, the dominant interaction being, not surprisingly, short-range repulsion and long-range attraction. Electrostatic interactions between the total charges of the segments, naturally specific to the interacting entities, are taken into account through a Coulomb potential. We note that PMFs were extracted from all-atom simulations in vacuum. If water was used, the size of simulated systems and, more importantly, the time required for the convergence, would increase strongly. Future investigations will have to compare in vacuum and in solvent PMFs and establish efficient methods for the calculation of the latter.

The MD program NAMD 2.5 (30) was used to simulate the CG system, with an implicit solvent model implemented. Three basic features of water are chosen to be represented by the implicit solvent, namely, viscosity, fluctuations due to Brownian motion, and dielectric permittivity. The relative dielectric constant is set to 80 everywhere. The effect of the liquid environment in our simulation is accounted for by the presence of frictional and fluctuating forces. This is done by solving for each bead the Langevin equation

$$m\ddot{r} = \mathbf{F} - \gamma\mathbf{v} + \psi(t).$$

Here, $\mathbf{r}$ is the position of the bead, $\mathbf{F}$ is the force acting on the bead from other beads in the system, γ is a damping coefficient controlling frictional forces (for bead velocity $\mathbf{v}$), and $\psi(t)$ is a temperature-dependent random force related to the frictional forces through the fluctuation-dissipation theorem. The scaling of the friction term with velocity, $-\gamma\mathbf{v}$, is key to our

modeling, particularly given that, as we apply a rotation to the filament, beads along the outer edges of the filament will experience the strongest force opposing motion. In effect, this means that the frictional effects of the solvent will apply a torque to the monomers in our system, the frictional torque pointing in the opposite direction to the torque that induces filament rotation. This frictional torque, arising mainly through the beads at the periphery since they move fastest on average, induces a rearrangement of the flagellum monomers as described in Results.

The motions of CG beads obey the Langevin equation, so aside from the potential energy-based forces between the beads, viscous damping and random forces from the solvent are introduced, with a single parameter defining the strength of both (see (30)); this parameter, the damping (or friction) constant γ, is directly related to the diffusion constant D, $D = k_{\mathrm{B}}T/(m\gamma)$, where k_{B} is the Boltzmann constant, T is the temperature, and m is the mass of the diffusing object. To select a proper γ-value, five all-atom MD simulations of single segments ($\sim$500 atoms each) of a monomer in a periodic water box were performed. The diffusion rate for every segment was then computed, resulting in γ-values in the range 12–15 ps^{-1}. The value $\gamma = 14$ ps^{-1} was accordingly used in our CG simulations (use of the Langevin equation, according to the fluctuation-dissipation theorem, allows one also to maintain a constant temperature, which we set to 300 K). Ions (CG beads carrying a charge of $25|e|$ and representing 25 Na^{+} ions each) were added to neutralize the total negative charge of the flagellum.

The velocities arising in the simulations and giving rise to frictional forces need to be compared with the average speed of free diffusion, to ensure that the employed frictional force model holds. In our simulations, the flagellar filament (20 nm in diameter) was rotated at a rate of 100 turns per millisecond, i.e., CG beads at the outer edge of the filament move by $\sim$6 nm in one μs. With $\gamma = 14$ ps^{-1} and average CG bead masses of 2000–4000 Da, the diffusion coefficient D is $\sim$50 nm^2/μs. According to the Einstein relation, the average displacement due to diffusion is then $\sim$7 nm in 1 μs. Thus, the velocities arising due to the rotation are on the same order of magnitude as those arising due to the diffusion at equilibrium, and the viscous force model employed is appropriate.

All-atom MD simulations performed to parameterize the CG model were carried out using the CHARMM22 force field (28) and NAMD 2.5. A cutoff of 12 Å was used for the nonbonded interactions, and the particle-mesh Ewald summation (grid step <1 Å) was employed for long-range electrostatics. Temperature (300 K) and pressure (1 atm) were controlled using Langevin dynamics with a damping constant of 5 ps^{-1} and a Nosé-Hoover Langevin piston with period of 100 fs and decay time of 50 fs. The integration timesteps were 1 fs, 2 fs, and 4 fs for bonded, nonbonded, and long-range electrostatic interactions, respectively.

The CG simulations (Table 1) were run with a single time step of 400 fs and 30 Å cutoff for nonbonded interactions. In most of the simulations, the flagellum filament (whole or a basal segment consisting of 30 unit proteins, see Table 1) was rotated with constant angular velocity; for this purpose, a harmonic force with spring constant of 5 kcal/(Å^2 mol) was applied to the

TABLE 1   CG simulations of the flagellar filament segments

Simulation	Description	Number of beads	Length (nm)	Simulation time (μs)
F1100swim	1100 units, ''run''	17,025	530	30.5
F1100tumble	1100 units, ''tumble''	17,025	530	30.5
F1100	1100 units, no rotation	17,025	530	27.6
F220swim	220 units, ''run''	3405	116	19.6
F220tumble	220 units, ''tumble''	3405	116	17.8
F220swim-ns	220 units, ''run,'' no solvent	3405	116	19.6
F220tumble-ns	220 units, ''tumble,'' no solvent	3405	116	20.7
F220swim-fast	220 units, ''run,'' full segment is rotated	3405	116	0.1
F220tumble-fast	220 units, ''tumble,'' full segment is rotated	3405	116	0.1

The segments, consisting of either 1100 or 220 protein monomers, are rotated with constant angular velocity of 100 turns per ms (1000 turns per ms in simulations F220swim-fast and F220tumble-fast), in the directions corresponding to either running (counterclockwise when looking down the filament axis toward the bacterial body) or tumbling (clockwise). The rotation is applied to the first 30 monomers at the bottom of the segment (the segment's end closer to the bacterial body in the full filament). In simulations F220swim-fast and F220tumble-fast the rotation is applied over the full segment length.

bottom part (relative to the orientation in Fig. 1 *a*) in each affected unit protein. Analysis and visualization were performed using VMD (31). All simulations used CG filament models created from an R-type straight filament (13) employing the methods described in this section.

Use of the CHARMM force field and of a simple implicit solvent model allowed us to employ the MD program NAMD without any changes to run the CG simulations. The scaling of the performance with an increasing number of processors for parallel runs was found to be the same as for average all-atom simulations with NAMD. As an example, for the 220-unit filament (which would require up to 15,000,000 atoms to simulate in an all-atom representation, water included), 2.8 μs were simulated in a day on a single 2.4 GHz Opteron processor. This performance, together with the 20,000-fold reduction in the system size (500-fold for the protein, but larger overall since we use an implicit solvent), allowed us to follow the dynamics of a macromolecular aggregate 0.5 μm in size over 30 μs.

RESULTS

The size and timescales necessary to study the bacterial flagellum only come within reach of molecular dynamics simulations when a coarse-grained description is applied. In any coarse-grained simulation, one must carefully consider which properties of a system are reproduced reasonably well at the level of detail present in the approach. In the case of the bacterial flagellar filament, we cannot expect to observe the switching interactions believed to be responsible for *L-R* transitions on a scale of a few Ångstroms. Instead, we use the present approach to focus on the large-scale behavior of the flagellar filament under torque, and its response to rotation in a viscous solvent. In addition, despite the large speedup of our coarse-grained approach, simulation of a functionally relevant event (at least one full rotation) during the 10-μs simulation time requires a rotation speed $\sim$500 times faster than that seen for *S. typhimurium* in nature (32). This difference in rotation speed must be kept in mind throughout the analysis of our results, and makes it difficult to draw any quantitative comparison between our results and experiments. Nevertheless, the qualitative behavior of the filament seen in our simulations already reveals several important insights.

Simulation of the coarse-grained filament in solvent (simulation F1100) in the absence of applied torque showed that the overall superstructure of the flagellar filament is stable in our model. However, the overall height of the filament decreased from 528 nm at the beginning to 495 nm and the average maximal radius (measured for the outermost bead of each turn) of the filament dropped from 9.6 nm to 8.9 nm. Both of these figures represent a roughly 7% decrease in dimension, indicating that our model may slightly underestimate the size of the filament components. The shrinking in length is due to the relatively small number of beads per monomer; increasing the number of beads should repair it. Despite this shrinking, the overall flagellum structure remained stable. For example, the RMSD value for a single ring of 11 monomers is 0.89 nm per bead and the protofilament twist per monomer increased from 4° to 4.6°, smaller than the $\sim$5° change (and switch in handedness) involved in a supercoiling transition (11). The RMSD value

of the individual monomers is 0.85 nm per bead; the close RMSD values of monomers and rings indicates a uniformity of the simulated structure. The height, angle, and RMSD values all change rapidly at the beginning of the simulation, but have stabilized completely after 15 μs.

Coiling of protofilaments and supercoiling of the flagellum

The structures of the filament in simulations F1100swim and F1100tumble, after 25 μs of dynamics, are shown in Fig. 3 *a*. As in the case of the unrotated filament, we do observe a slight shortening in both cases, with the height dropping to 511 nm in F1100tumble and 509 nm in F1100swim. The
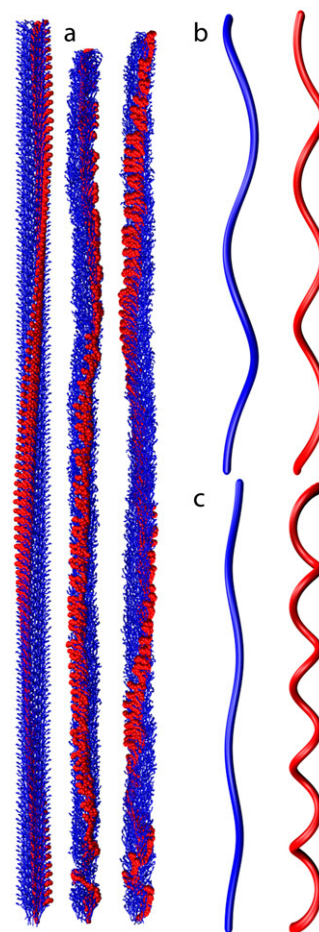

FIGURE 3 Coiling and supercoiling of the 1100-monomer flagellar filament segment in our simulations. (*a*) Full view of the starting structure (*left*), conformation of the segment after 25 μs in simulation F1100swim (*center*), and after 25 μs in simulation F1100tumble. In each case a single protofilament is highlighted in red to illustrate the protofilament coiling. (*b*) Schematic view of the supercoiling observed after 25 μs in simulations F1100swim (*blue*) and F1100tumble (*red*), with an exaggerated supercoil diameter to better illustrate the nature of the helix. Helical parameters were determined as discussed in the text. (*c*) Schematic view (as in *b*) of supercoil models, constructed using the bistable protofilament model with protofilament heights and angles obtained from our simulations.

overall structure of the filament is preserved in each case, and the average internal RMSD of the monomers is 0.93 nm in F1100swim and 0.94 nm in F1100tumble. It must be noted that in both of these simulations, the rotated section of the filament begins to tear away from the rest of the assembly after roughly 20 μs; after this point the rotated region is able to slip along the interface with the rest of the filament and, thus, fails to fully transmit the rotational force. This tearing is almost certainly caused by the fact that the filament in these simulations is rotated 500 times faster than physiological flagella (32), and thus is exposed to much greater drag than a normal flagellum would be. Because of this, for the purposes of the following analysis all snapshots and data are taken up through 20 μs of simulation unless otherwise noted.

Both the coiling and supercoiling characteristics of the flagella from these simulations are represented in Fig. 3. Panel *a* highlights (through coloring) the coiling of a single (equivalent) protofilament over the length of the filament as described by our simulations. One can recognize that individual protofilaments form right-handed helices both in the initial structure and in simulation F1100tumble, whereas in the case of F1100swim a left-handed helix is found in the lower half of the filament, and a right-handed helix (similar to the initial configuration) through the remainder. The presence of right-handed protofilament coiling upon rotation in the tumbling direction and left-handed coiling for the swimming simulation is consistent with the experimental structures of 11-R and 11-L flagella; below, we examine the mechanism for inducing this change. In the region affected by this change, the rotation about the filament axis per monomer in a protofilament was on average $-7.89°$ in F1100swim and $17.49°$ in F1100tumble, compared with $4°$ in the starting structure. In contrast, in simulation F1100, this value remained under $4.6°$ throughout the simulation, indicating that the rotation was the primary cause of the changing twist. The fact that the left-handed coil occurs only halfway up the length of the filament from simulation F1100swim indicates that the influence of the rotation at the base of the filament did not propagate up the entire length of the model filament during our simulations.

The propagation speed of the motion can be estimated by checking the angular position (about the filament axis) of monomers throughout the length of the filament; monomers which have not yet been affected by the rotation, and all those in simulation F1100, show oscillations about a roughly constant value, whereas those affected by the rotation show a linear relationship between angular position and time. By this metric, motion in F1100swim had propagated 492 nm along the length of the filament in 20 μs, and that in F1100tumble propagated 494 nm during the same time period, giving a propagation rate of 2.5×10^4 μm/s (it is not surprising that our observation of the helical reversal in F1100swim lags behind this figure, since it will take some time after the rotation begins to reverse the handedness of a given area of protofilaments).

There is no experimentally measured quantity that should correspond directly to this propagation; for the sake of perspective, it can be compared to the overall transition rate of full flagellar filaments, but this should not be expected to match well. Turner and co-workers observed flagellar filaments 6 μm in length to undergo the complete transition from normal to curly I states in 0.1 s (33); this gives a propagation rate for the complete transition of 60 μm/s, which is much slower than the calculated rate.

The supercoiling states of the filaments from simulations F1100swim and F1100tumble are shown in Fig. 3 *b*. Pitch data from our simulations was extracted by plotting the position of a bead corresponding to the interface between the D_0 and D_1 domains (denoted the D_0D_1 bead; compare to Fig. 1) of greatest radius from the filament axis in 40 Å slices along this axis. In both cases, this supercoiled region appeared in an area several nanometers past the edge of the rotated monomers, and ended at or before the leading edge of rotational propagation. As seen in Fig. 3 *b*, the filament from simulation F1100swim forms a relatively long-pitch left-handed supercoil, whereas the filament from F1100tumble forms a shorter pitch right-handed supercoil. The difference in handedness between these supercoils matches that observed between the normal and curly I/II supercoils (8,9), but the high rotation speed applied in these simulations makes it unreasonable to compare simulations and experimental results in quantitative terms.

Protofilament contacts and heights

The polymorphic supercoiling of the flagellar filament is correlated with switching of several protofilaments between L- and R-forms, which have been found to have different repeat distances (52.7 Å and 51.9 Å, respectively) (7,10). A supercoiled filament then arises from the curvature generated by the presence of these repeat distances in the protofilaments; for example, a filament with two R-type protofilaments and nine L-type protofilaments (2R/9L) forms the normal configuration involved in the running mode, whereas the 5R/6L and 6R/5L combinations form curly states thought to be involved in the tumbling-mode (9,33). Recent MD studies have suggested the presence of switch-interactions between neighboring monomers, which arise between monomers involved in L-state (long) protofilaments, but are broken between R-state (short) protofilaments (7,12); using these switch-interactions as a criterion for identifying protofilaments as L- or R-state lead to the observation of the expected 2R/9L, 5R/6L, and 6R/5L states even in systems containing only 44 monomers (12).

The average rise per monomer for each of the 11 protofilaments for simulations F1100swim and F1100tumble is shown in Fig. 4 (calculated as the rise between D_0D_1 beads; see Fig. 1 *a*); in each case the data was calculated above the region of the filament being directly twisted, and <30 turns up the filament, to ensure that calculations were
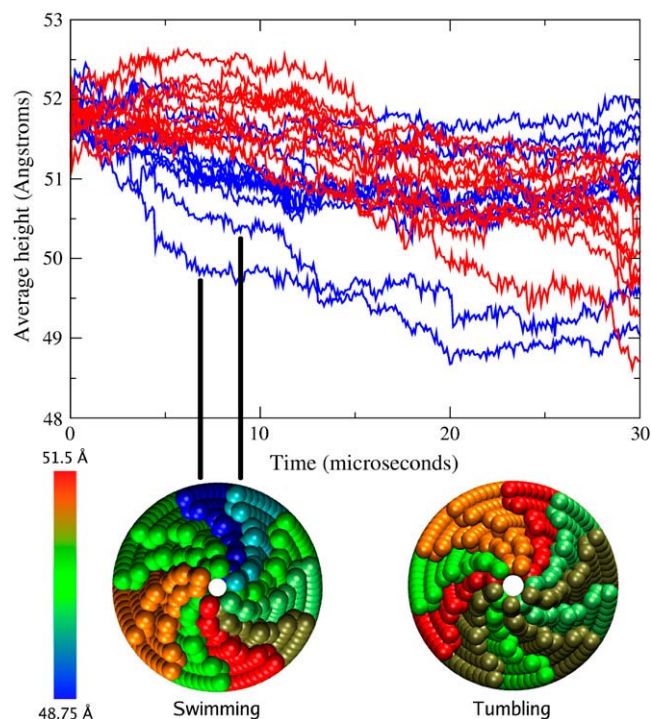
FIGURE 4 Average rise per monomer for each of the 11 protofilaments, calculated for F1100swim (*blue*) and F1100tumble (*red*). Protofilament wheel diagrams (*bottom*) show the heights of the protofilaments for both simulations after 20 μs, on a scale from 48.75 Å (*blue*) to 51.5 Å (*red*).

performed on a region consistently influenced by the turning. For simulation F1100swim beginning after 10 μs, one can recognize in Fig. 4 two distinct populations of protofilaments, one set of nine protofilaments with an average rise of 51.5 Å per monomer, and the other set of two protofilaments with an average rise of 49.5 Å. The protofilaments from simulation F1100tumble, in contrast, show a slightly broader distribution of heights, but do not have the same clear distinction between protofilament types; the average protofilament height after 20 μs is 50.8 Å in this case. It should be noted that the figures given here are for rise per monomer along the filament axis, not along the protofilament direction; it turns out that taking the measurement along the filament axis is more robust under the rotation conditions of our simulations. The difference of the stated experimental 52.7:51.9 Å (for L- and R-forms) and simulated 51.5:49.5 Å figures is due to the different measurement directions.

While the protofilament heights calculated from our simulations are shorter than experimental values, qualitative insight can still be obtained by comparing the relative lengths of protofilaments in this model with idealized configurations (7). In the case of F1100swim, we observe nine L-type protofilaments and two R-type protofilaments (2R/9L); furthermore, as seen in the bottom panel of Fig. 4, the two short protofilaments are adjacent to each other. This should not be surprising, as it is sensible for the shorter protofilaments to be co-located on the interior face of the supercoil, an arrange-

ment also found in the bistable protofilament model (11). In the case of simulation F1100tumble, there is no obvious distinction between L-type and R-type protofilaments; however, the protofilament wheel diagram in Fig. 4 does reveal that the four highest height protofilaments cluster along one face of the filament (along with a single moderate height protofilament), a configuration similar to the experimental curly II (6R/5L) state.

For both the swimming and tumbling states found here, supercoiling parameters can be constructed from the protofilament heights and angular displacements using the procedure of Hasegawa and co-workers (11) and assuming the average height and angular displacement values for each L- or R-state cluster found in each of the simulations. Supercoils built using these parameters are shown in Fig. 3 *c*. The results indicate that the supercoiling observed in our simulations indeed arises from a mechanism similar to that seen in the bistable protofilament model, suggesting that solvent effects induce switching in the filament. Slower rotation is necessary to verify this.

Effect of the solvent

The results of our simulations of the 1100-unit filament demonstrate how coiling of the protofilaments and supercoiling of the flagellum arise along the filament's length. To investigate this behavior further, we studied a five-times shorter flagellum segment in simulations F220swim and F220tumble. We found that the speed of rotation propagation, switching of the protofilament states, and supercoiling of the segment are the same (within ~10%) as in simulations F1100swim and F1100tumble, respectively. This demonstrates that the behavior of the flagellum is due to local interactions.

The function of the flagellum is to propel the bacterium, by pushing against the surrounding solvent, and thus, one may further probe how much of a role the solvent plays in driving local interactions to alter the quaternary structure of the flagellum. To address this question, we simulated a 220-unit flagellum segment in a nonviscous medium using a reduced γ-value of 2 ps^{-1} (simulations F220swim-ns and F220tumble-ns). We found that without solvent (i.e., with reduced friction) the flagellum rotates essentially as a rigid body, i.e., the relative positions of monomers are frozen.

The results of simulations F220swim-ns and F220tumble-ns are compared with those of F220swim and F220tumble in Fig. 5 *a*. Two representative protofilaments, highlighted in blue and red, maintain their initial helical conformation (to within ±0.5° per monomer) throughout simulations F220swim-ns and F220tumble-ns. In the presence of solvent (friction), the right-handed helix, which the corresponding protofilaments form, becomes shorter when the segment is rotated in the tumbling direction, and the helix becomes left-handed when rotated in the running direction. Enlarged snapshots from the simulations of the entire 1100-unit filament in solvent (Fig. 5 *b*) reveal protofilament arrangements very similar to those
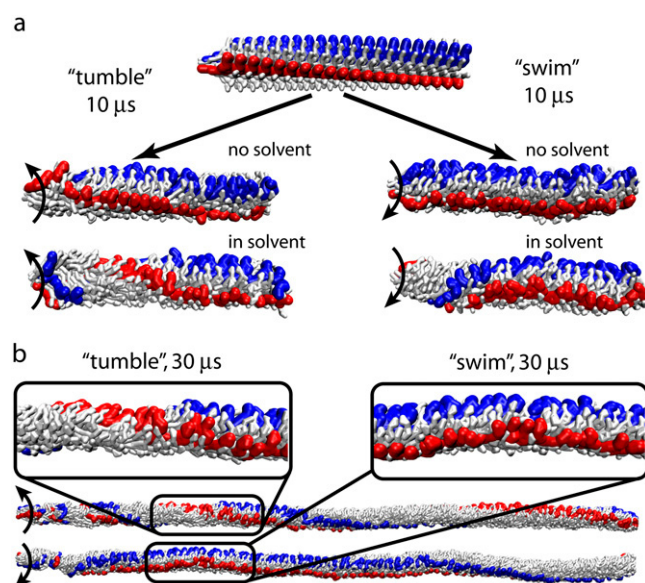
FIGURE 5 Effect of solvent on rotation of the flagellar filament. Two protofilaments out of 11 are shown in red and blue. Snapshots from the simulations of 220-monomer segments (F220swim, F220tumble, F220swim-ns, F220tumble-ns) are presented in panel *a*. When simulated with low friction ($\gamma = 2$ ps^{-1}, F220swim-ns and F220tumble-ns), denoted here as *no solvent*, the segment rotates as a whole, and the arrangement of the protofilaments remains the same as in the initial structure, independent of the rotation direction (compare top three snapshots in *a*). When solvent is present, i.e., with the friction constant $\gamma = 14$ ps^{-1}, torque propagation through the segment is much slower, and the protofilament arrangement changes depending on the rotation direction. For example, in the bottom-right snapshot in panel *a*, the protofilaments rearranged into a left-handed helical conformation instead of the right-handed one. The same behavior is observed in the simulations of longer filament segments (1100 monomers) in solvent (*b*).

arising in simulations of the 220-unit segment in solvent. Thus, it is clear that the solvent (friction) plays a crucial role in the switching between the arrangements of protofilaments and, consequently, in producing supercoiling along the entire filament.

We also performed simulations where the rotation was 10 times faster than in other runs and was applied over the whole filament length (simulations F220tumble-fast and F220swim-fast; see Supplementary Material). The rotated segment behaved very differently depending on the rotation direction, brushing-out for the tumbling mode, and becoming very smooth for the running mode (which is not surprising since the monomers have intrinsic clockwise curl when looked upon down the flagellum axis toward the bacterium; see Fig. 1), with the shape of the monomers being strongly affected by the rotation. In similar simulations without solvent (friction), segments looked the same for both rotation directions. In simulations with slower rotation applied to the filament base (F1100swim, F1100tumble, F220swim, F220tumble), the difference due to rotation one way or another was not in the monomer shape (which was basically unaffected by the rotation), but in the mutual arrangement of monomers. This indicates that the role of the solvent

(friction) is not a direct coiling or uncoiling of the filament by rubbing against its ragged surface, but rather a facilitation of proper torque transfer over the filament (by providing friction), allowing the monomers to rearrange and produce the coiling that corresponds to either tumbling or running.

The coarseness of our model and the overly fast rotation of the flagellum certainly introduce artifacts into the observed behavior, but nevertheless the role of filament-solvent interactions in protofilament rearrangement and filament geometry suggested by our simulations is likely significant. To our knowledge, the effect of solvent on flagellum supercoiling under conditions of running or tumbling has not been systematically investigated before. Our study suggests that both the structure of the flagellum and the effect of the liquid medium (viscous drag) are important for understanding the polymorphic transitions controlling bacterial swimming.

CONCLUSION

We have presented a study of the bacterial flagellum by means of numerical simulations. For this purpose, we developed a CG MD technique with parameters extracted systematically from a well-established all-atom simulation. The CG approach allowed us to investigate the dynamics of a 0.5-μm long flagellar filament over 30 μs. We found that the model flagellum supercoils when rotated, and that this supercoiling results from solvent effects (friction) on the flagellar protofilaments, which alter their local arrangement. The measured pitch of the supercoil for the rotation direction corresponding to running is almost two times longer than that for tumbling. Furthermore, we noted that the interactions between solvent and flagellar proteins are extremely important for the functional characteristics of the flagellum: without solvent, i.e., without viscous drag, rearrangement of protofilaments and supercoiling do not arise. This observation shows that the behavior of the flagellum is determined not only by the interprotein interactions, but also by hydrodynamic effects, suggesting that future studies of the flagellar filaments should further address the details of interactions between filament and solvent.

While the results of our study are in qualitative agreement with experimental data, quantitative comparison is not yet successful due to the high rotation speed required because of our $\sim$10-μs simulation time-limit. In addition, the present model lacks a description of the detailed switching interactions between protofilaments. Overcoming this omission requires a multiscale coarse-graining methodology, in that different levels of detail need to be combined in a single CG description. Such multiscale resolution is possible for the CG scheme we used since the neural computation method employed here permits the resolution of a hierarchy of spatial properties (25).

The CG technique applied in our study has been developed in a general form, which allows one to employ it directly to investigate other macromolecular systems. The

CG simulations can be carried out with the program NAMD, achieving a parallel computing performance in line with all-atom simulations. Therefore, concepts and methods developed for all-atom simulations can be transferred to CG simulations. With presently available computing resources, the new CG method is capable of simulating systems on a micrometer length-scale and soon on a microsecond timescale.

SUPPLEMENTARY MATERIAL

An online supplement to this article can be found by visiting BJ Online at http://www.biophysj.org.

REFERENCES

1. DePamphilis, M. L., and J. Adler. 1971. Purification of intact flagella from *Escherichia coli* and *Bacillus subtilis*. *J. Bacteriol.* 105:376–383.

2. Larsen, S. H., R. W. Reader, E. N. Kort, W.-W. Tso, and J. Adler. 1974. Change in direction of flagellar rotation is the basis of the chemotactic response in *Escherichia coli*. *Nature*. 249:74–77.

3. Macnab, R. M., and M. K. Ornston. 1977. Normal-to-curly flagellar transitions and their role in bacterial tumbling. Stabilization of an alternative quaternary structure by mechanical force. *J. Mol. Biol.* 112:1–30.

4. Kamiya, R., S. Asakura, K. Wakabayashi, and K. Namba. 1979. Transition of bacterial flagella from helical to straight forms with different subunit arrangements. *J. Mol. Biol.* 131:725–742.

5. Mimori, Y., I. Yamashita, K. Murata, Y. Fujiyoshi, K. Yonekura, C. Toyoshima, and K. Namba. 1995. The structure of the R-type straight flagellar filament of *Salmonella* at 9 Å resolution by electron cryomicroscopy. *J. Mol. Biol.* 249:69–87.

6. Morgan, D. G., C. Owen, L. A. Melanson, and D. J. DeRosier. 1995. Structure of bacterial flagellar filaments at 11 Å resolution: packing of the α-helices. *J. Mol. Biol.* 249:88–110.

7. Samatey, F. A., K. Imada, S. Nagashima, F. Vonderviszt, T. Kumasaka, M. Yamamoto, and K. Namba. 2001. Structure of the bacterial flagellar protofilament and implications for a switch for supercoiling. *Nature*. 410:331–337.

8. Asakura, S. 1970. Polymerization of flagellin and polymorphism of flagella. *Adv. Biophys.* 1:99–155.

9. Calladine, C. R. 1978. Change of waveform in bacterial flagella: the role of mechanics at the molecular level. *J. Mol. Biol.* 118:457–479.

10. Yamashita, I., K. Hasegawa, H. Suzuki, F. Vonderviszt, Y. Mimori-Kiyosue, and K. Namba. 1998. Structure and switching of bacterial flagellar filaments studied by x-ray fiber diffraction. *Nat. Struct. Biol.* 5:125–132.

11. Hasegawa, K., I. Yamashita, and K. Namba. 1998. Quasi- and non-equivalence in the structure of bacterial flagellar filament. *Biophys. J.* 74:569–575.

12. Kitao, A., K. Yonekura, S. Maki-Yonekura, F. A. Samatey, K. Imada, K. Namba, and N. Go. 2006. Switch interactions control energy frus-

13. Yonekura, K., S. Maki-Yonekura, and K. Namba. 2003. Complete atomic model of the bacterial flagellar filament by electron cryomicroscopy. *Nature*. 424:643–650.

14. Wang, Y., A. J. Rader, I. Bahar, and R. L. Jernigan. 2004. Global ribosome motions revealed with elastic network model. *J. Struct. Biol.* 147:302–314.

15. Trylska, J., V. Tozzini, and J. A. McCammon. 2005. Exploring global motions and correlations in the ribosome. *Biophys. J.* 89:1455–1463.

16. Tama, F., and C. L. Brooks III. 2005. Diversity and identity of mechanical properties of icosahedral viral capsids studied with elastic network normal mode analysis. *J. Mol. Biol.* 345:299–314.

17. Tozzini, V., and A. McCammon. 2005. A coarse grained model for the dynamics of flap opening in HIV-1 protease. *Chem. Phys. Lett.* 413:123–128.

18. Chu, J.-W., and G. A. Voth. 2005. Allostery of actin filaments: molecular dynamics simulations and coarse-grained analysis. *Proc. Natl. Acad. Sci. USA.* 102:13111–13116.

19. Marrink, S. J., A. H. de Vries, and A. E. Mark. 2004. Coarse-grained model for semiquantitative lipid simulations. *J. Phys. Chem. B.* 108:750–760.

20. Marrink, S. J., J. Risselada, and A. E. Mark. 2005. Simulation of gel phase formation and melting in lipid bilayers using a coarse-grained model. *Chem. Phys. Lipids.* 135:223–244.

21. Shelley, J. C., M. Y. Shelley, R. C. Reeder, S. Bandyopadhyay, P. B. Moore, and M. L. Klein. 2001. Simulations of phospholipids using a coarse-grain model. *J. Phys. Chem. B.* 105:9785–9792.

22. Lopez, C., P. Moore, J. Shelley, M. Shelley, and M. Klein. 2002. Computer simulation studies of biomembranes using a coarse-grain model. *Comput. Phys. Commun.* 147:1–6.

23. Shih, A. Y., A. Arkhipov, P. L. Freddolino, and K. Schulten. 2006. Coarse-grained protein-lipid model with application to lipoprotein particles. *J. Phys. Chem. B.* 110:3674–3684.

24. Shih, A. Y., P. L. Freddolino, A. Arkhipov, and K. Schulten. 2006. Assembly of lipoprotein particles revealed by molecular dynamics simulations. *J. Struct. Biol.* In press.

25. Ritter, H., T. Martinetz, and K. Schulten. 1992. Textbook: Neural Computation and Self-Organizing Maps: An Introduction. Revised English Ed. Addison-Wesley, New York.

26. Martinetz, T., and K. Schulten. 1991. A ''neural gas'' network learns topologies. *In* Artificial Neural Networks. T. Kohonen, K. Mäkisara, O. Simula, and J. Kangas, editors. Elsevier, Amsterdam.

27. Martinetz, T., and K. Schulten. 1994. Topology-representing networks. *Neural Networks.* 7:507–522.

28. MacKerell, A. D. Jr., D. Bashford, M. Bellott, R. L. Dunbrack Jr., J. Evanseck, M. J. Field, S. Fischer, J. Gao, H. Guo, S. Ha, D. Joseph, L. Kuchnir, et al. 1998. All-atom empirical potential for molecular modeling and dynamics studies of proteins. *J. Phys. Chem. B.* 102:3586–3616.

29. Bahar, I., M. Kaplan, and R. L. Jernigan. 1997. Short-range conformational energies, secondary structure propensities, and recognition of correct sequence-structure matches. *Protein Struct. Funct. Gen.* 29:292–308.

30. Phillips, J. C., R. Braun, W. Wang, J. Gumbart, E. Tajkhorshid, E. Villa, C. Chipot, R. D. Skeel, L. Kale, and K. Schulten. 2005. Scalable molecular dynamics with NAMD. *J. Comput. Chem.* 26:1781–1802.

31. Humphrey, W., A. Dalke, and K. Schulten. 1996. VMD—visual molecular dynamics. *J. Mol. Graph.* 14:33–38.

32. Kudo, S., Y. Magariyama, and S.-I. Aizawa. 1990. Abrupt changes in flagellar rotation observed by laser dark-field microscopy. *Nature*. 346:677–680.

33. Turner, L., W. S. Ryu, and H. C. Berg. 2000. Real-time imaging of fluorescent flagellar filaments. *J. Bacteriol.* 182:2793–2801.